Journal of Materials Chemistry C

PAPER

View Article Online
View Journal | View Issue

Cite this: J. Mater. Chem. C, 2019, 7, 10918

Ultrathin yttrium fluoride nanostructures: controlled synthesis and polarized up-conversion emission property†

G. Murali,[a] Sandeep Kaur,[b] Jongwoo Kim,[c] Sang Hwan Nam,[c] Joong Hee Lee,[a] Yung Doug Suh,[de] Insik In *[a] and Seung Hee Lee *[b]

Received 24th June 2019,
Accepted 6th August 2019

DOI: 10.1039/c9tc03403j

rsc.li/materials-c

Ultrathin nanomaterials are very significant members of the nanocrystalline material family because of their unique properties of broad significance. In the present study, highly uniform atomically thick YF_3 nanobelts and nanowires are fabricated by using an oleylamine assisted colloidal chemical strategy. Reaction monitoring demonstrates that two-dimensional lamellar assemblies of YF_3 clusters are vital intermediates in the growth process, which transform to ultrathin nanobelts and nanowires depending on the heating temperature. This approach can be readily extended to produce ultrathin structures of other lanthanide fluoride (ErF_3, YbF_3, TmF_3, NdF_3, and LaF_3) systems. The polarized upconversion emission of Yb^{3+}/Er^{3+} co-doped YF_3 is demonstrated for a domain of a perfectly aligned assembly of parallel ultrathin nanowires. The polarization degree of green, red and infrared emission peaks are 0.32, 0.28 and 0.50, respectively.

1. Introduction

Ultrathin nanostructures, which have at least one dimension in the sub-5 nm regime, are currently in the spotlight of materials research owing to their unexpected and unprecedented properties compared to their larger size nanomaterial counterparts.[1–3] Given the significant difficulty in controlling the growth rates of crystal facets at such low dimensions, it has been challenging to the science and art of crystal growth to produce ultrathin nanostructures of various functional materials. Colloidal synthesis has played a seminal role in exploring the one and two-dimensional (1D and 2D) ultrathin nanostructures of various functional bulk materials such as metal chalcogenides, metals, metal organic frameworks, *etc.*[4–12] However, the research progress in the panorama of ultrathin nanostructures is quite limited. Unearthing the synthetic conditions for producing ultrathin nanostructures of a wide variety of functional materials is important for fundamental scientific research and potentially can lead to new possibilities in the fields of energy, environment and biomedicine research.

Lanthanide compounds have attracted an enormous amount of research interest due to their unique optical, electrical and magnetic properties underpinning their promising applications in various fields.[13–16] Although many kinds of lanthanide compound structures were prepared, the ultralong 1D structure is greatly beneficial for specified applications. For example, Rui Ye *et al.* demonstrated near-infrared (NIR) upconversion (UC) lasing in Er–Y chloride silicate nanowires under the excitation of 1476 nm laser at room temperature.[17] Shi Hu *et al.* reported macromolecule like properties in the case of ultrafine GdOOH and EuOOH nanostructures.[18] Lanthanide fluorides are among the most studied lanthanide compounds due to their higher efficiencies of photon UC arising from their low phonon energies.[19,20] It has recently been proven that 1D UC nanocrystals are capable of uplifting the polarization emission property.[21,22] In view of this, synthesis of extremely directional ultrathin nanostructures of various lanthanide fluorides and investigating their polarization emission properties are beneficial.

Yttrium fluoride (YF_3) has gained extensive research interest for its high UC efficiency[23–25] as well as for its merits in energy harvesting,[26] color displays,[27] bioimaging[28] and photocatalysis.[29] Size and shape are two typical parameters for controlling the

[a] Department of Polymer Science and Engineering, Department of IT Convergence (BK21 PLUS), Chemical Industry Institute, Korea National University of Transportation, Chungju 27469, South Korea. E-mail: In1@ut.ac.kr
[b] Applied Materials Institute for BIN Convergence, Department of BIN Convergence Technology, Department of Polymer-Nano Science and Technology, Chonbuk National University, Jeonju 54896, South Korea. E-mail: lsh1@chonbuk.ac.kr
[c] Center for Convergent Research of Emerging Virus Infection, Korea Research Institute of Chemical Technology (KRICT), Daejeon 34114, South Korea
[d] Bio Platform Technology Research Center, Therapeutics & Biotechnology Division, Korea Research Institute of Chemical Technology (KRICT), Daejeon 34114, South Korea
[e] School of Chemical Engineering, Sungkyunkwan University, Suwon 16419, South Korea

† Electronic supplementary information (ESI) available. See DOI: 10.1039/c9tc03403j

UC performance of YF_3 micro/nanocrystals.[25,30] A variety of synthetic routes have been developed to produce YF_3 with specific shapes, including nanorod,[30] zigzag-shaped nanorod,[31] nanowire,[32] sphere,[33] flower,[34,35] rhombic disk,[32,36] rectangular nanoplate,[24] diamond,[37] octahedral,[37] truncated octahedral,[37] dumbbell,[25] hexagon,[25] spindle and bundle.[38] Despite the mounting interest, the difficulty in controlling YF_3 into 1D nanocrystals has impeded the exploration of anisotropic growth related properties and applications. Recently, we have found a synthetic method for 1D YF_3:Yb^{3+}/Er^{3+} nanorods and tailored the emission efficiency by controlling the aspect ratio of nanocrystals using various inorganic salts.[30] Here, we present a simple and effective colloidal synthesis strategy for the fabrication of highly uniform ultrathin 1D YF_3 nanostructures and studied their polarization UC emission property. Besides YF_3, we have also demonstrated that this synthesis approach can be employed to yield ultrathin structures of other lanthanide fluorides, including ErF_3, YbF_3, TmF_3, NdF_3 and LaF_3, signifying that this approach is general and could be useful for the synthesis of other nanostructures *via* colloidal synthesis.

2. Experimental section

2.1 Materials

$YCl_3{\cdot}6H_2O$, $YbCl_3{\cdot}6H_2O$, $ErCl_3{\cdot}6H_2O$, $TmCl_3{\cdot}6H_2O$, $NdCl_3{\cdot}6H_2O$, $LaCl_3{\cdot}7H_2O$, NH_4F, 1-octadecene (ODE), oleylamine (OM), octylamine, dodecylamine, oleic acid (OA), and trioctylphosphine (TOP) were purchased from Sigma-Aldrich (St. Louis, MO, USA). All the reagents were used as received without further purification.

2.2 Synthesis of undoped and Yb^{3+}/Er^{3+} doped ultrathin YF_3 nanostructures

Ultrathin YF_3 nanostructures were synthesized according to our earlier report with slight modifications.[30] In a typical synthesis, $YCl_3{\cdot}6H_2O$ (0.303 g, 1 mmol), OM (3 mL), and ODE (17 mL) were added into a 50 mL three-neck round-bottom flask with subsequent heating at 160 °C for 30 min. The reaction mixture was then cooled to room temperature (25 °C) and 10 mL of a methanol solution containing NH_4F (0.1111 g, 3 mmol) was added into the flask. The mixed solution was stirred for 30 min and then heated at 120 °C to remove methanol. Once methanol was completely evaporated, the reaction mixture was heated to 220–280 °C under a N_2 atmosphere. After a specific reaction time (*e.g.*, 0.5 h, 1 h, 2 h, and 8 h), aliquots of samples were collected. The nanocrystals were precipitated by centrifugation (10 000 rpm, 5 min) and purified by washing twice with ethanol. Purified nanocrystals were dispersed in ethanol for the subsequent experiments. To synthesize Yb^{3+}/Er^{3+} doped YF_3 ultrathin nanostructures, 1 mmol of rare-earth chlorides with the Y : Yb : Er composition of 78 : 20 : 2 was added, while maintaining other experimental conditions at fixed values.

2.3 Characterization

The crystallinity of the nanostructures was determined by X-ray powder diffraction (XRD) using a MAX-2500 instrument and Fe-filtered Cu-Kα radiation (λ = 1.54 Å). The products were characterized by high-resolution transmission electron microscopy (HRTEM) (HITACHI H-7650 and JEOL JEM-2010) and field emission scanning electron microscopy (FESEM; SU-70, Hitachi). The photoluminescence (PL) was recorded using a homemade microscope equipped with a spectrometer and a NIR laser (980 nm). The sample was irradiated by a 980 nm laser from a single-mode laser diode (AC1401-0600-980-SM, EM4) under wide-field imaging. The PL spectra were measured from the emitted beam passing through the microscope by a CCD camera (PIXIS400BR, Princeton Instruments) equipped with a spectrograph (SCT320, Princeton Instruments). To investigate the polarization UC emission, a 980 nm laser with 38 mW power and 2.5 $\times$ 10^7 W cm^{-2} power density was utilized.

3. Results and discussion

3.1 Ultrathin YF_3 nanobelts and nanowires

In wet chemical synthetic methods, the anisotropic morphology of the lanthanide fluoride nanocrystals is critically decided by two important parameters, one is the surface energy associated with each facet of the given crystal and the other is the surfactant employed in the synthesis. During the growth, the high surface energy facet leads anisotropic growth while the surfactant adhering to the budding crystal suppresses the growth of other facets by blocking monomer access. However, achieving a highly anisotropic ultrathin lanthanide fluoride nanocrystal structure such as nanowires and nanobelts is still challenging. In particular, regarding the nanobelt morphology, which requires the growth of two slightly different energy facets, no acceptable progress has been reported to date. The reason for this could be that the conventional synthesis of lanthanide fluoride nanocrystals using high boiling solvents is usually carried out at a high temperature of 310 °C, and this high thermal energy input into the reaction medium offsets the small surface energy difference between the two lateral facets. Therefore, to investigate the build-up of nanobelt morphology of YF_3, we have carried out the reaction at a relatively low temperature of 240 °C using OM surfactant, which is promising for inducing anisotropic growth.

At this low reaction temperature (240 °C), TEM images of aliquots taken after 2 h presented certain chemical fusing of reactants with the formation of no meaningful morphology (Fig. S1a, ESI†). After 4 h, the anisotropic structure evolving from the fused reactants can be clearly recognized (Fig. S1b, ESI†). Further reaction at 240 °C for 8 h produced flexible nanobelts with the lateral dimensions of 16.2 $\pm$ 3.9 nm and a length on the micrometer scale (Fig. 1a–c and Fig. S1c, ESI†). As shown in Fig. 1c, some of the nanobelts were found to stack face to face on their edges due to van der Waals interaction between the ligands on the surface of the nanobelts. These stacked nanobelts enabled us to measure the thickness, which is about 2.5 $\pm$ 0.2 nm (Fig. S1d, ESI†). Although all these structures are grown at a relatively low temperature (240 °C), HRTEM proves the single crystalline state of the structures, clearly showing the lattice fringes with an inter planar spacing of 0.34 nm corresponding

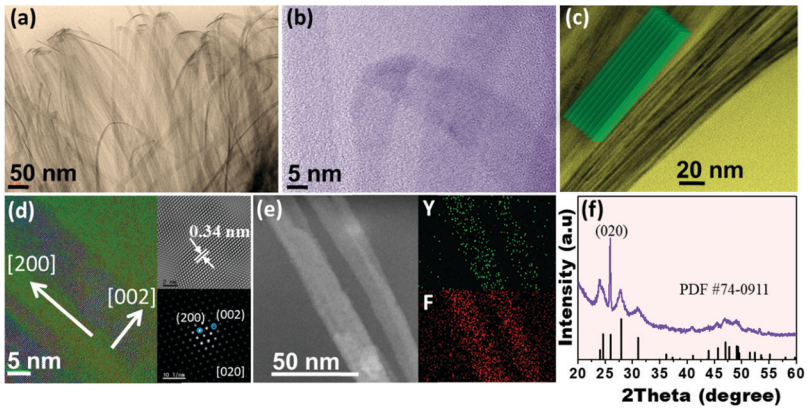

Fig. 1 (a–c) TEM images, (d) HRTEM and SAED images, (e) STEM-based EDS mapping profiles for Y and F, and (f) XRD pattern of nanobelts.

to the (200) plane of YF_3 (Fig. 1d). The SAED pattern shown in Fig. 1d confirms that YF_3 nanobelts possess [200], [002] and [020] as longitudinal, lateral and thickness growth directions, respectively. The low growth temperature of 240 °C makes the miniature energy difference between the{200} facets more evident. The glued amine ligands onto the surface of the nanobelts, *i.e.*, to the (020) facet, significantly hinder the nanobelt growth along the thickness direction. The STEM image and corresponding EDS maps of YF_3 nanobelts clearly confirm the flat surface and the uniform presence of both Y and F elements throughout the nanobelts (Fig. 1e). The XRD pattern of the YF_3 nanobelts matches that of the orthorhombic phase and shows obvious broadened peaks compared to those of bulk YF_3 (Fig. 1f). The observed strong and narrow (020) peak further confirms that ultrathin nanobelts exhibit the (020) plane as a flat surface (Fig. 1f). A decrease in the reaction temperature from 240 °C to 220 °C required a longer reaction time of 20 h to generate partially grown nanobelts along with loosely associated 1D aggregates (Fig. S2, ESI†).

When the reaction temperature was increased to 260 °C, nanobelts were found to form rather quickly within 2 h (Fig. 2a). However, the width of the nanobelts decreased slightly to 11.6 ± 2.3 nm, while the thickness increased to 3.5 ± 0.4 nm (Fig. S3a and b, ESI†). Aliquots taken at 30 min interval of the reaction traced the underlying growth mechanism of these ultrathin structures (Fig. 2b, c and Fig. S3c, ESI†). As shown in Fig. 2b, initially, tiny YF_3 nanocrystals with sizes ranging from 6–10 nm (equal to several YF_3 unit cells in dimension) are assembled into one big cage-like geometry that is believed to fully incorporate OM in it. The SAED pattern of the 1D cage reveals that these structures are single crystalline in nature and HRTEM analysis reveals that these tiny crystals possess (200) and (002) planes as basal and side facets, respectively (Fig. 2c, d and Fig. S3c, ESI†). It is believed that as the reaction progresses, these tiny nanocrystals will aggregate loosely *via* the (200) facets to form a necklace like embryo of 1D structure and meanwhile the growth along (002) extends the lateral dimension of the embryo (Fig. 2d). The joints of these nanocrystals are evident in Fig. 2d. The continuation of growth results in ripening of aggregates and is reasoned to lead to the formation of ultrathin nanobelts (Fig. 2a). On the other hand, the OM surfactant glued to the (020) planes prevents the crystalline growth along this direction and separates the individual nanobelts by its hydrocarbon chain length (~2 nm).

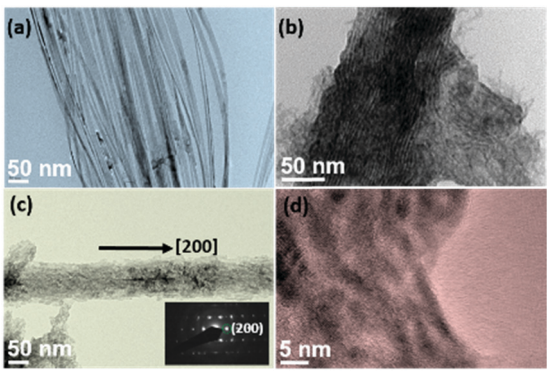

Fig. 2 (a) TEM image of nanobelts synthesized at 260 °C with 2 h reaction time. (b–d) TEM images of the sample extracted at 30 min of reaction time.

Fig. 3a–d and Fig. S4a (ESI†) compare YF_3 nanocrystals synthesized with different reaction times at 280 °C. As shown in Fig. 3a and b, the sample taken at 30 min of reaction time is composed of distinct ultrathin nanowires self-assembled in domains, where each domain holds dozens of perfectly aligned parallel ultrathin nanowires. Ultrathin nanowires are more or less uniform in diameter with an average diameter of 4.5 ± 0.7 nm while the length extends up to several micrometers (Fig. S4b, ESI†). As the reaction time increases to 1 h, nanowires were unbundled to individual nanowires with an increased diameter of 9.4 ± 1.7 nm (Fig. S4c, ESI†). Interestingly, when the reaction time is increased further to 2 h, nanowires turned into short nanorods (Fig. 3d). Similarly the breakdown behavior of long nanowires into short nanorods has been observed in the case of metal nanowires with the explanation based on Rayleigh–Plateau instability theory.[39] According to this theory, a cylindrical structure tends to break down when the force from the surface tension surpasses the plastic flow limit of a structure. The theory estimated the critical length above which a nanowire becomes unstable as $L = 2\pi r$ (r: radius of the wire). Here, at a reaction time of 1 h, the critical length of the nanowire estimated

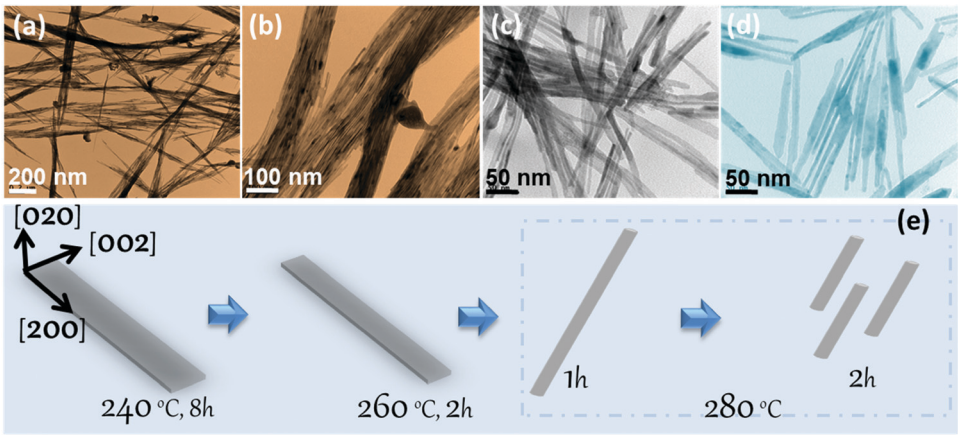

Fig. 3 TEM images of sample synthesized at 280 °C with a reaction time of (a and b) 30 min, (c) 1 h, and (d) 2 h. (e) Schematic representation of the morphology transformation with increasing reaction temperature from 240 °C to 280 °C.

from the formula, 29.5 ± 5.3 nm ($r \sim 4.7 \pm 0.85$ nm), is less than the observed experimental value. Therefore, YF_3 nanowires, which are longer than the critical length, become unstable as the reaction progresses and break down into shorter nanorods. Further, as shown in Fig. 3e, it is believed that the increased growth temperature suppressed the growth along the (002) plane and triggered the morphological transformation from nanobelts to nanowires.

3.2 The role of the surfactant and precursor composition

Given that the fluoride precursor plays a pivotal role in the morphological evolution of UC nanocrystals, we investigate the effect of varied NH_4F concentration in the reaction mixture by keeping other experimental parameters constant at 280 °C (Fig. 4 and Fig. S5, ESI†). For the case of 5 mmol of NH_4F, the obtained aliquots at 30 min showed an aggregated morphology composed of spherical particles with a large size disparity (Fig. 4a). Particle diameters are extended up to hundreds of nanometers (Fig. 4a). The transparency of particles at close examination revealed that these particles are not composed of a solid interior; instead, they are formed through the wrapping of thin layered structures and resemble fullerene-like structures (Fig. 4b and c). When observed using SEM, the particles appeared to be crumpled spheres with an uneven surface as many knoll's extended throughout the surface (Fig. 4d and e). The uneven surface appears as alternate bright and dark regions in the TEM image of a particle (Fig. 4b and e). Interestingly, the HRTEM observation shows that the thin layered structures are network-like agglomerated nanoparticles (Fig. 4c). An increase in the reaction time to 2 h, induced a morphological transformation from fullerene-like structures to irregular shape nanocrystals (Fig. S5a and b, ESI†). If the NH_4F concentration reaches 7 mmol and 9 mmol, nanoplates and a mixture of nanoparticles and nanoplates are afforded from the fused reactants, respectively (Fig. S5c–f, ESI†). To further confirm the influence of NH_4F concentration on the evolution of anisotropic structures, different NH_4F contents (5, 7 and 9 mmol) were also employed in the reaction that yielded a nanobelt morphology at a reaction temperature of 260 °C. Aggregated nanoparticle clusters are generated from the fused reactants for all NH_4F concentrations (Fig. S6a–f, ESI†). Therefore, it can be deduced that the increased NH_4F concentration hampers the YF_3 lamellar template formation and the growth of elongated nanostructures from the fused reactants. In addition, when KF or NaF replaces NH_4F as a fluoride source at 280 °C with other reaction conditions remaining unchanged, nanostructures quite different from those observed using NH_4F as a fluoride source emerged (Fig. S7, ESI†). The KF fluoride source induces nanoparticles with a bipyramidal shape, while NaF produces clusters of nanoparticles and nanorods. These results confirm that, among the three different fluoride sources, NH_4F is significant to induce the anisotropic growth.

A surfactant-dependent investigation was performed to explore the ligand role in the formation process of nanowires. A reaction conducted with TOP surfactant did not produce nanoparticles with a wire morphology, only irregular shape aggregated particles were observed (Fig. S8a, ESI†); while in the case of OA, small rhombic plates are formed (Fig. S8b, ESI†).

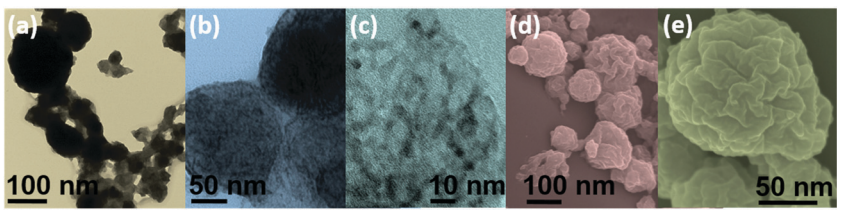

Fig. 4 (a–c) TEM and (d and e) SEM images of YF_3 nanostructures prepared at 280 °C and 30 min reaction time with $F^-/Y^{3+} = 5$.

Interestingly, the mixture of OM and OA in 1 : 1 ratio produced elongated plates, which are irregular in shape and resemble dogbone shaped structures (Fig. S8c, ESI†). The combination of OM : OA : TOP in 1 : 1 : 1 ratio produces star like nanoparticles with a varied number of legs (Fig. S8d, ESI†). Amorphous, orthorhombic and cubic crystalline structures are observed for TOP, OA and OM:OA, and OM:OA:TOP surfactants, respectively (Fig. S8e, ESI†). From the above results, it can be deduced that TOP, OM and OA selectively adsorb onto crystalline planes of budding nanoparticles and alter the growth pathway of nanoparticles to form various geometries, as shown in Fig. S8a–d (ESI†). Importantly, the use of other functional groups either solely or in combination with amine does not result in a cage-like 2D lamellar geometry that promotes the anisotropic ultrathin structures (Fig. S8a–d, ESI†). Further, OM quantity influencing the morphology was also investigated. At 260 °C, 100% OM as solvent yielded a nanoplate morphology whose width increased with increasing the reaction time (Fig. S9a and b, ESI†). On the other hand, at 280 °C, the solvent compositions 15ODE:5OM and 12ODE:8OM resulted in a nanorod morphology, and the length of the nanorod is smaller when compared to the nanorod obtained with 17ODE:3OM (Fig. 3d and Fig. S9c, d, ESI†).

To gain more insight, amines with different hydrocarbon chain lengths were employed in the reaction. The results obtained using octylamine ($C_8H_{19}N$) and dodecylamine ($C_{12}H_{27}N$) as surfactants can be seen in (Fig. S10, ESI†). Irrespective of the chain length, both the amines produced a nanowire bundle morphology at 30 min and the length of the wires varied substantially in both the samples (Fig. S10a and c, ESI†). Further, the wire as well as bundle morphology synthesized using octylamine is stable even after 2 h of reaction time, whereas dodecylamine produced wires that broke down into shorter nanorods similar to the OM ($C_{18}H_{37}N$) case (Fig. S10b and d, ESI†). The distance between two adjacent wires in the assembly of wires seemed to depend on the hydrocarbon chain length of the amine functional group employed. The shorter the chain length, the closer they are assembled and the harder it is to separate into individual nanowires.

3.3 The growth mechanism of ultrathin nanostructures

From the experimental results, it is concluded that all experimental parameters including reaction temperature and time, surfactant, and precursor composition are crucial in producing the anisotropic ultrathin nanowires and nanobelts. The growth of these anisotropic YF_3 nanocrystals from the solution is seemingly composed of two steps: (1) the reaction of long-chain primary amines and precursor salts resulted in a coalescence of nuclei into 2D lamellar assemblies and the (2) anisotropic growth of YF_3 ultrathin structures is guided by the oriented attachment (Fig. 5). Alkylamine is observed to be crucial in the formation of lamellar clusters, as the other surfactants including OA, TOP, OA:OM and TOP:OM:OA resulted in regular growth of nanoparticles with peculiar morphology without cluster formation.

At the beginning of nanocrystal growth, the reaction of precursor ions with the alkylamine depletes the free alkylamine in the reaction medium. To minimize the alkylamine interaction with the solvent, the generated organic–inorganic mixture (OM-precipitate) self-organizes into lamellar clusters.[40,41] These lamellar clusters composed of alternating layers of precipitate passivated with alkylamine (Fig. 5). The uniform spacing between the precipitates is ensured by the van der Waals forces between the hydrocarbon amine chains attached to the precipitates. Thereafter, within the layers, the nanocrystal growth is guided by the oriented attachment. When small particles with no or less surfactant on the preferred high energy facet come together, the facets join together and rearrange their crystallography to form a big 1D nanowire or nanobelt (Fig. 5). Eventually, highly oriented bunches of ultrathin nanostructures were grown within the cluster. Upon prolonged reaction, the cluster disintegrated into individual 1D nanostructures.

3.4 UC photoluminescence and polarization emission property

To investigate the UC emission properties, Yb^{3+}/Er^{3+} co-doped YF_3 ultrathin nanostructures were prepared (Fig. S11, ESI†). The UC PL spectra of YF_3:Yb^{3+}/Er^{3+} nanowires and nanobelts under the illumination of a 980 nm continuous wave diode laser are shown in Fig. 6a. Both the morphologies exhibited identical emission profiles with three well resolved emission bands centered at 545 nm (green), 660 nm (red) and 810 nm (infra-red), which correspond to the $^2H_{11/2}/^4S_{3/2} \rightarrow {}^4I_{15/2}$, $^4F_{9/2} \rightarrow {}^4I_{15/2}$, and $^4I_{9/2} \rightarrow {}^4I_{15/2}$ transitions of Er^{3+} ions, respectively.[42,43]

To investigate the polarization emission property of YF_3:Yb^{3+}/Er^{3+} nanowires, the light emission from the aligned parallel nanowire

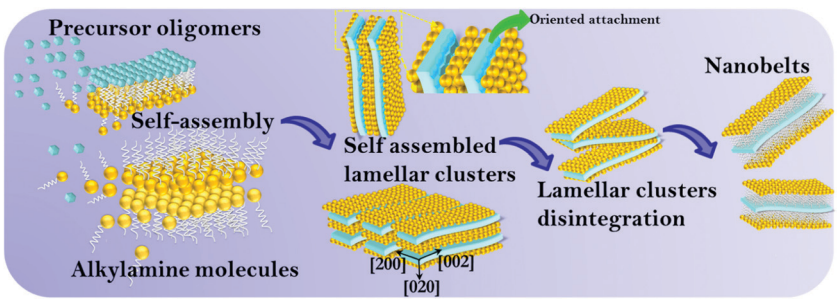

Fig. 5 A schematic illustration of the growth of YF_3 nanobelts. Gold color spheres represent the surfactant molecules, and the blue color species indicate the YF_3 nuclei.

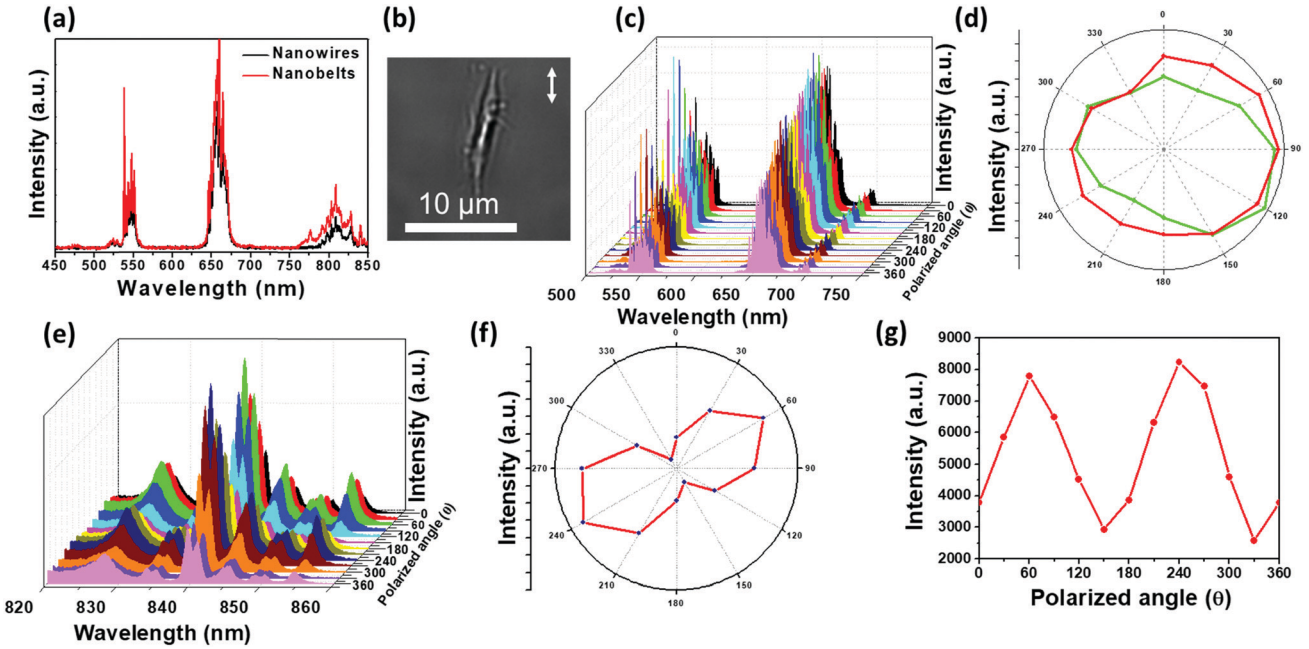

Fig. 6 (a) Photoluminescence spectra of YF_3:Yb^{3+}/Er^{3+} nanowires and nanobelts. (b) A representative bright-field image of a YF_3:Yb^{3+}/Er^{3+} nanowire bundle. (c) Green and red UC luminescence spectra and corresponding (d) polar plots as a function of emission polarization angle for a single nanowire bundle shown in (b). (e) NIR UC emission spectra, and corresponding (f) polar plot and (g) emission intensity as a function of the emission polarization angle for a nanowire bundle (b).

bundle under the linearly polarized excitation was allowed to pass through a half-wave-plate to the detector. The intensity of the UC emission profile fluctuates when the polarization of emission is rotated from 0° to 360°, indicating the existence of emission polarization (Fig. 6b–g).[44] Importantly, the infra-red emission peak (800–850 nm) showed a greater periodic dependence on the polarization of emission than the green and red emission peaks (Fig. 6e–g). Fascinatingly, the maximum infra-red emission intensity was observed at a polarization angle of 60°. To understand this unusual behavior, further investigations including theoretical modelling are needed. To quantitatively analyze the polarization state of the emission peaks, a parameter called polarization degree (ρ) is defined as: $\rho = (I_{max} - I_{min})/(I_{max} + I_{min})$, where I_{max} and I_{min} are the maximum and minimum emission intensities.[45] The polarization degrees for the green, red and infrared emission peaks are 0.32, 0.28, and 0.50, respectively.

3.5 Synthesis of other lanthanide fluoride ultrathin nanostructures using current synthesis strategy

The current synthetic strategy was extended to produce ultra-thin structures of other lanthanide fluorides, such as ErF_3, YbF_3, TmF_3, NdF_3 and LaF_3. Morphologies obtained for these fluorides are shown in the representative TEM images of Fig. 7a–e. For orthorhombic crystalline structured ErF_3, YbF_3 and TmF_3, a solvent composition of 17 : 3 ODE : OM remains suitable to achieve uniform ultrathin nanostructures at 260 °C (Fig. 7a–c and f). The observed morphology for ErF_3 is nanowires, while the nanobelt morphology is obtained for YbF_3 and TmF_3. On the other hand, hexagonal crystalline structured

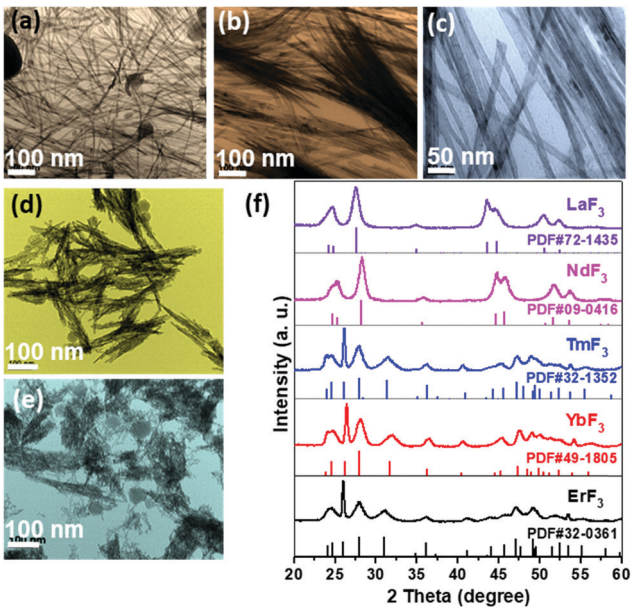

Fig. 7 TEM images of ultrathin (a) ErF_3 (b) YbF_3 and (c) TmF_3 nanostructures synthesized at 260 °C with ODE/OM = 17 : 3. TEM images of (d) NdF_3 and (e) LaF_3 ultrathin nanostructures synthesized at 260 °C with 20 mL of OM solvent. (f) XRD patterns of nanostructures shown in (a–e).

NdF_3 and LaF_3 exhibit an irregular nanoplate and nanorod morphology with 17ODE:3OM solvent composition, respectively (Fig. S12, ESI†). However, the use of 100% OM solvent yielded clusters of 1D zigzag nanostructures for both NdF_3 and LaF_3 (Fig. 7d–f).

4. Conclusions

In conclusion, we have successfully developed a robust synthetic strategy to produce ultrathin YF_3 nanostructures. Ultrathin YF_3 nanowires, nanobelts, and fullerene like spheres were synthesized by systematically controlling the reaction parameters. We observed that lamellar templates are formed from the precursor ions of YF_3 and OM. As the reaction progresses, the YF_3 nanoclusters entrained within the lamellar template transform into ultrathin nanostructures. The increase in reaction temperature from 240 °C to 280 °C diminishes the lateral dimension growth of the nanostructure, *i.e.*, the (002) plane, and this is the reason for the transformation of the nanostructure morphology from nanobelt to nanowire. The polarization UC emission study on the self-assembled aligned YF_3:Yb/Er nanowires demonstrates that the emission intensity varies with the polarization angle of detection. The estimated polarization degree for green, red and infrared emission peaks is 0.32, 0.28, and 0.50, respectively. Finally, our strategy and results will open up new avenues to exploit diverse ultrathin morphologies of other materials, as well as evoking inspiration in the polarization emission studies in lanthanide systems.

Conflicts of interest

There are no conflicts of interest to declare.

Acknowledgements

This research was supported by the Basic Science Research Program through the National Research Foundation of Korea (NRF) funded by the Ministry of Education (2018R1A6A1A03023788, 2016R1D1A1B01007189). This work was also supported by the Global Research Laboratory (GRL) Program through the National Research Foundation of Korea (NRF) funded by the Ministry of Science and ICT (no. 2016911815) and the National Research Council of Science & Technology (NST) grant by the Korea government (MSIT) (CRC-16-01-KRICT).

References

1 X. Huang, X. Qi, F. Boey and H. Zhang, Graphene-based composites, *Chem. Soc. Rev.*, 2012, **41**, 666–686.
2 Z. Zeng, Z. Yin, X. Huang, H. Li, Q. He, G. Lu, F. Boey and H. Zhang, Single-layer semiconducting nanosheets: high-yield preparation and device fabrication, *Angew. Chem., Int. Ed.*, 2011, **50**, 11093.
3 H. Zhang, Ultrathin two-dimensional nanomaterials, *ACS Nano*, 2015, **9**(10), 9451.
4 Y. Du, Z. Yin, J. Zhu, X. Huang, X. J. Wu, Z. Zeng, Q. Yan and H. Zhang, A general method for the large-scale synthesis of uniform ultrathin metal sulphide nanocrystals, *Nat. Commun.*, 2012, **3**, 1177.
5 G. Jia and U. Banin, A general strategy for synthesizing colloidal semiconductor zinc chalcogenide quantum rods, *J. Am. Chem. Soc.*, 2014, **136**(31), 11121.
6 N. Li, L. Qin, H. Zhao, Z. Liu, X. Zhang, Y. Zheng and Y. Du, High quality ultrathin lanthanide selenide nanostructures with dual modal functionalities, *Chem. Mater.*, 2016, **28**(8), 2507.
7 H. Yang, S. W. Finefrock, J. D. A. Caballero and Y. Wu, Environmentally benign synthesis of ultrathin metal telluride nanowires, *J. Am. Chem. Soc.*, 2014, **136**(29), 10242.
8 Z. Huo, C.-k. Tsung, W. Huang, X. Zhang and P. Yang, Sub-two nanometer single crystal Au nanowires, *Nano Lett.*, 2008, **8**, 2041.
9 B. H. Hong, S. C. Bae, C.-W. Lee, S. Jeong and K. S. Kim, Ultrathin single-crystalline silver nanowire arrays formed in an ambient solution phase, *Science*, 2001, **294**, 348.
10 Z. Fan, X. Huang, C. Tan and H. Zhang, Thin metal nanostructures: synthesis, properties and applications, *Chem. Sci.*, 2015, **6**, 95.
11 S. Zhao, Y. Wang, J. Dong, C. T. He, H. Yin, P. An, K. Zhao, X. Zhang, C. Gao, L. Zhang, J. Lv, J. Wang, J. Zhang, A. M. Khattak, N. A. Khan, Z. Wei, J. Zhang, S. Liu, H. Zhao and Z. Tang, Ultrathin metal–organic framework nanosheets for electrocatalytic oxygen evolution, *Nat. Energy*, 2016, **1**, 16184.
12 Y. Peng, Y. Li, Y. Ban, H. Jin, W. Jiao, X. Liu and W. Yang, Metal-organic framework nanosheets as building blocks for molecular sieving membranes, *Science*, 2014, **346**, 1356.
13 C. Liu, Z. Gao, J. Zeng, Y. Hou, F. Fang, Y. Li, R. Qiao, L. Shen, H. Lei, W. Yang and M. Gao, Magnetic/upconversion fluorescent NaGdF4:Yb,Er nanoparticle-based dual-modal molecular probes for imaging tiny tumors in vivo, *ACS Nano*, 2013, **7**(8), 7227.
14 O. Yamamoto, Y. Takeda, R. Kanno and M. Fushimi, Thermal decomposition and electrical conductivity of $M(OH)_3$ and MOOH (M = Y, lanthanide), *Solid State Ionics*, 1985, **17**, 107.
15 G. Chen, H. Qiu, P. N. Prasad and X. Chen, Upconversion nanoparticles: design, nanochemistry, and applications in theranostics, *Chem. Rev.*, 2014, **114**, 5161.
16 J. Zhou, Q. Liu, W. Feng, Y. Sun and F. Li, Upconversion luminescent materials: advances and applications, *Chem. Rev.*, 2015, **115**, 395.
17 R. Ye, C. Xu, X. Wang, J. Cui and Z. Zhou, Room-temperature near-infrared up-conversion lasing in single-crystal Er-Y chloride silicate nanowires, *Sci. Rep.*, 2016, **6**, 34407.
18 S. Hu, H. Liu, P. Wang and X. Wang, Inorganic nanostructures with sizes down to 1 nm: a macromolecule analogue, *J. Am. Chem. Soc.*, 2013, **135**(30), 11115.
19 H. X. Mai, Y. W. Zhang, L. D. Sun and C. H. Yan, Highly efficient multicolor up-conversion emissions and their mechanisms of monodisperse $NaYF_4$:Yb,Er core and core/shell-structured nanocrystals, *J. Phys. Chem. C*, 2007, **111**, 13721.
20 H. X. Mai, Y. W. Zhang, R. Si, Z. G. Yan, L. D. Sun, L. P. You and C. H. Yan, High-quality sodium rare-earth fluoride nanocrystals: controlled synthesis and optical properties, *J. Am. Chem. Soc.*, 2006, **128**, 6426.
21 S. Shi, L. D. Sun, Y. X. Xue, H. Dong, K. Wu, S. C. Guo, B. T. Wu and C. H. Yan, Scalable direct writing of

lanthanide-doped $KMnF_3$ perovskite nanowires into aligned arrays with polarized up-conversion emission, *Nano Lett.*, 2018, **18**(5), 2964.

22 J. Zhou, G. Chen, E. Wu, G. Bi, B. Wu, Y. Teng, S. Zhou and J. Qiu, Ultrasensitive polarized up-conversion of Tm^{3+}–Yb^{3+} doped β-$NaYF_4$ single nanorod, *Nano Lett.*, 2013, **13**(5), 2241.

23 C. X. Li, J. Yang, P. P. Yang, H. Z. Lian and J. Lin, Hydrothermal synthesis of lanthanide fluorides LnF_3 (Ln = La to Lu) nano-/microcrystals with multiform structures and morphologies, *Chem. Mater.*, 2008, **20**, 4317.

24 G. Murali, B. H. Lee, R. K. Mishra, J. M. Lee, S. H. Nam, Y. D. Suh, D. K. Lim, J. H. Lee and S. H. Lee, Synthesis, luminescence properties, and growth mechanisms of YF_3:Yb^{3+}/Er^{3+} nanoplates, *J. Mater. Chem. C*, 2015, **3**, 10107.

25 G. Murali, S. Kaur, Y. C. Chae, M. Ramesh, J. Kim, Y. D. Suh, D. K. Lim and S. H. Lee, Monodisperse, shape-selective synthesis of YF_3:Yb^{3+}/Er^{3+} nano/microcrystals and strong upconversion luminescence of hollow microcrystals, *RSC Adv.*, 2017, **7**, 24255.

26 J. Wu, J. Wang, J. Lin, Y. Xiao, G. Yue, M. Huang, Z. Lan, Y. Huang, L. Fan, S. Yin and T. Sato, Dual functions of YF_3:Eu^{3+} for improving photovoltaic performance of dye-sensitized solar cells, *Sci. Rep.*, 2013, **3**, 2058.

27 H. Guan, Y. Sheng, Y. Song, C. Xu, X. Zhou, K. Zheng, Z. Shi and H. Zou, YF_3:RE^{3+} (RE = Dy, Tb, Eu) Sub-microstructures: controllable morphology, tunable multicolor, and thermal properties, *J. Phys. Chem. C*, 2017, **121**, 23080.

28 Y. J. Xu, J. Lin, Y. Lu, S. L. Zhong, L. Wang, L. Dong, Y. D. Wu, J. Peng, L. Zhang, X. F. Pan, W. Zhou, Y. Zhao, L. P. Wen and S. H. Yu, Lanthanide co-doped paramagnetic spindle-like mesocrystals for imaging and autophagy induction, *Nanoscale*, 2016, **8**, 13399.

29 Z. Li, C. Li, Y. Mei, L. Wang, G. Dua and Y. Xiong, Synthesis of rhombic hierarchical YF_3 nanocrystals and their use as upconversion photocatalysts after TiO_2 coating, *Nanoscale*, 2013, **5**, 3030.

30 G. Murali, R. K. Mishra, J. M. Lee, Y. C. Chae, J. Kim, Y. D. Suh, D. K. Lim and S. H. Lee, Aspect-ratio controlled synthesis and tunable luminescence of YF_3:Yb^{3+}/Er^{3+} upconversion nanocrystals, *Cryst. Growth Des.*, 2017, **17**, 3055.

31 H. Li, Q. Huang, Y. Wang, K. Chen, J. Xie, Y. Pan, H. Su, X. Xie, L. Huang and W. Huangab, Sc^{3+}-induced morphology, phase structure, and upconversion luminescence evolution of YF_3:Yb/Er nanocrystals, *J. Mater. Chem. C*, 2017, **5**, 6450.

32 T. Paik, A. M. Chacko, J. L. Mikitsh, J. S. Friedberg, D. A. Pryma and C. B. Murray, Shape-controlled synthesis of isotopic yttrium-90-labeled rare earth fluoride nanocrystals for multimodal imaging, *ACS Nano*, 2015, **9**(9), 8718.

33 B. Shao, Q. Zhao, Y. Jia, W. Lv, M. Jiao, W. Lu and H. You, Facile large-scale synthesis of monodisperse REF_3 (RE = Y, Ce, Nd, Sm-Lu) nano/microcrystals and luminescence properties, *J. Mater. Chem. C*, 2014, **2**, 7666.

34 S. Wang, S. Song, R. Deng, H. Guo, Y. Lei, F. Cao, X. Li, S. Su and H. Zhang, Hydrothermal synthesis and upconversion photoluminescence properties of lanthanide doped YF_3 sub-microflowers, *CrystEngComm*, 2010, **12**, 3537.

35 S. Sarkar and V. Mahalingam, Tuning the crystalline phase and morphology of the YF_3:Eu^{3+} microcrystals through fluoride source, *CrystEngComm*, 2013, **15**, 5750.

36 H. Qiu, G. Chen, R. Fan, L. Yang, C. Liu, S. Hao, M. J. Sailor, H. Ågren, C. Yang and P. N. Prasad, Intense ultraviolet upconversion emission from water-dispersed colloidal YF_3:Yb^{3+}/Tm^{3+} rhombic nanodisks, *Nanoscale*, 2014, **6**, 753.

37 B. Shao, Q. Zhao, N. Guo, Y. Jia, W. lv, M. Jiao, W. Lu and H. You, YF_3:Eu^{3+} micro-single crystals: fine morphological tuning and luminescence properties, *Cryst. Growth Des.*, 2013, **13**, 3582.

38 L. Yan, W. Gao, Q. Han, X. Li, R. Wang, C. Zhang, M. Zhang, L. Wang and H. Zheng, Investigation on YF_3:Eu^{3+} architectures and their luminescence properties, *CrystEngComm*, 2015, **17**, 8242.

39 H. G. Liao and H. Zheng, Liquid cell transmission electron microscopy study of platinum iron nanocrystal growth and shape evolution, *J. Am. Chem. Soc.*, 2013, **135**(13), 5038.

40 M. R. Friedfeld, J. L. Stein and B. M. Cossairt, Main-group-semiconductor cluster molecules as synthetic intermediates to nanostructures, *Inorg. Chem.*, 2017, **56**(15), 8689.

41 Y. H. Liu, F. Wang, Y. Wang, P. C. Gibbons and W. E. Buhro, Lamellar assembly of cadmium selenide nanoclusters into quantum belts, *J. Am. Chem. Soc.*, 2011, **133**(42), 17005.

42 G. A. Kumar, M. Pokhrel, A. Martinez, R. C. Dennis, I. L. Villegas and D. K. Sardar, Synthesis and spectroscopy of color tunable Y_2O_2S:Yb^{3+},Er^{3+} phosphors with intense emission, *J. Alloys Compd.*, 2012, **513**, 559.

43 G. A. Kumar, M. Pokhrel, A. Martinez and D. K. Sardar, Synthesis and upconversion spectroscopy of Yb Er doped M_2O_2S (M = La, Gd, Y) phosphors, *Sci. Adv. Mater.*, 2012, **4**, 623.

44 P. Chen, M. Song, E. Wu, B. Wu, J. Zhou, H. Zeng, X. Liu and J. Qiu, Polarization modulated upconversion luminescence: single particle vs. few-particle aggregates, *Nanoscale*, 2015, **7**, 6462.

45 S. Kaur, G. Murali, R. Manda, Y. C. Chae, M. Yun, J. H. Lee and S. H. Lee, Functional film with electric-field-aided aligned assembly of quantum rods for potential application in liquid crystal display, *Adv. Opt. Mater.*, 2018, **6**(17), 1800235.